Particle Accelerators, 1991, Vol. 35, pp. 101–128
Reprints available directly from the publisher
Photocopying permitted by license only

ELECTROMAGNETIC STABILITY REGIMES IN A HELICAL QUADRUPOLE FOCUSING ACCELERATOR

C. M. TANG, P. SPRANGLE, J. KRALL, P. SERAFIM* AND F. MAKO†

Beam Physics Branch, Plasma Physics Division, Naval Research Laboratory, Washington, DC 20375–5000, USA.

(Received 15 November 1989; in final form 16 July 1990)

A number of high-current accelerator designs utilize strong focusing in the form of helical quadrupole and axial guide fields. We obtain a linear dispersion relation for a cold electron beam propagating in a perfectly conducting cylindrical waveguide subject to helical quadrupole and longitudinal magnetic fields, electromagnetic waveguide modes and image fields. The electromagnetic waveguide modes are expressed in terms of right-hand and left-hand circularly polarized waves. We find that the electron beam centroid, depending on the system parameters, can be i) orbit-unstable independent of the waveguide modes, ii) three-wave unstable, or iii) fully stable. Analytic expressions for the various stability conditions are obtained in the limit of zero beam current, where the right-hand and left-hand circularly polarized waves decouple. Algebraic expressions for the growth rate in each of the three-wave unstable regimes are presented. The full dispersion relation is solved numerically with results that are in good agreement with both the stability conditions and the growth rate expressions.

1. INTRODUCTION

A number of recent high-current accelerator configurations utilize strong focusing fields. These fields, consisting of a stellarator field (or helical quadrupole field) and an axial guide field, increase considerably the energy mismatch tolerance of the device and provide confining forces against the beam space charge forces.[1,2] The use of strong focusing fields has a potential difficulty in that they can lead to various types of beam instabilities, particularly the three-wave instability in which the externally imposed helical quadrupole field interacts with the transverse motion of the beam centroid to excite a transverse-electric (TE) waveguide mode.[3] We note that other instabilities can arise in such systems. It has been suggested, for example, that the helical quadrupole field may act like a wiggler field as in the free-electron laser.[4,5]

Two devices that utilize such strong focusing fields are the modified betatron accelerator (MBA)[6] and the spiral line induction accelerator (SLIA).[7–9] The recent addition of strong focusing to the MBA at the Naval Research Laboratory has allowed that accelerator to successfully accelerate a 0.9–1 kA beam to 15–16 MeV

* Northeastern University, Boston, MA 02115
† FM Technologies, Inc., Alexandria, VA 22304

for $\simeq 38{,}000$ turns in a vacuum chamber with resistive walls.[10] Interestingly enough, the three-wave instability appears to be absent in the MBA as a result of a low growth rate and the low Q of the MBA vacuum chamber. The SLIA, to be constructed by Pulse Sciences, Inc., will utilize the strong focusing for transport along the curved sections of the beam line between the accelerating cavities.

In the present paper we will focus our attention on the three-wave instability for which an approximate stability condition has recently been found.[11] Here we wish to obtain detailed analytical conditions for the various stability regimes and thus specify parameter ranges for which stable transport of an electron beam is feasible.

The dynamics of the electromagnetic waveguide modes and the beam modes associated with a relativistic electron beam propagating under the influence of external strong focusing fields will be analyzed. We will proceed by specifying the electromagnetic waveguide modes in terms of right-hand (RHCP) and left-hand (LHCP) circularly polarized waves. This formulation is intuitively motivated by the mathematical form of the helical quadrupole field. It is justified by the fact that the instability does not require that the RHCP and LHCP modes be simultaneously excited. In the simpler case when only the RHCP *or* the LHCP mode is excited, we obtain growth rates in agreement with case of coupled RHCP and LHCP modes to within a few percent in all but the most extreme (high-current) cases.

The dispersion relation for such a system is generated in Section II below. In Section III, we show that this dispersion relation, in the limit of zero beam current, gives analytical conditions for the various stability regimes. We find a) two physically distinct three-wave unstable regimes, b) two three-wave stable regimes and c) a regime in which the particle orbits themselves are unstable, irrespective of the electromagnetic waves. The orbit unstable regime is a recovery of an earlier result.[1,2] In addition, we obtain algebraic expressions for the growth rates in each of the three-wave unstable regimes. This is done with a simplified dispersion relation in which the RHCP and LHCP waves are decoupled and is valid in the low current regime. These are found to be in general agreement with the approximate expressions given in Ref. 12. Numerical solutions of the dispersion relation are presented in Section IV. The analytic expressions of the growth rates and stability boundaries are in good agreement with the numerical results of the dispersion relation.

2. MODEL

In our model the external fields consist of a periodic helical quadrupole field and a longitudinal magnetic field (see Figure 1). The electron beam radius is assumed to be small compared to the waveguide radius. In the equilibrium position, the beam is centered along the axis of a circular waveguide and the beam electrons are assumed to be monoenergetic with zero transverse velocity. Perturbing electromagnetic waveguide fields cause the beam centroid to develop a transverse velocity and become displaced off the z-axis. This displacement of the beam centroid amounts to a transverse macroscopic current which, under certain conditions, further excites the electromagnetic field. The displacement of the beam centroid also induces image

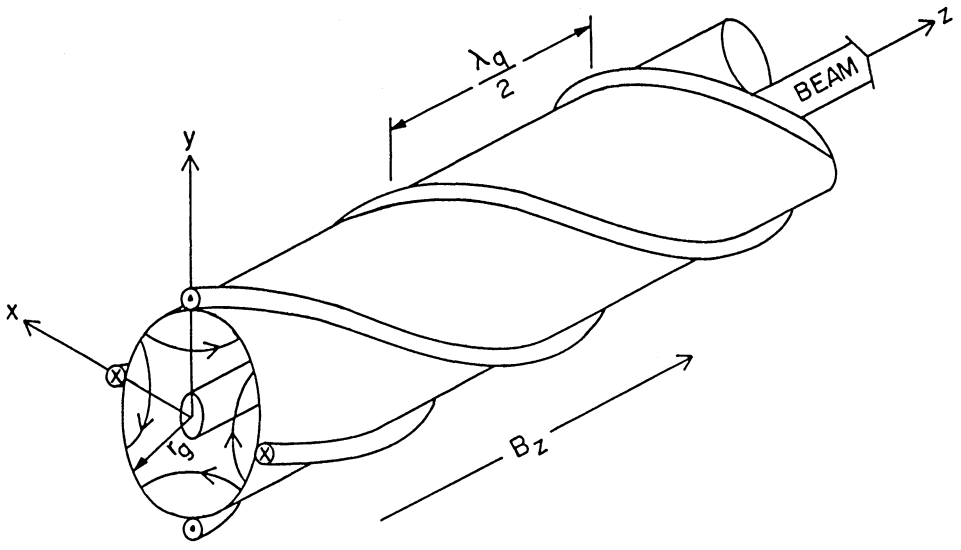

FIGURE 1 The geometry showing the conducting cylindrical drift tube, the helical quadrupole field and the axial guide field.

electric and magnetic fields on the wall of the waveguide. The beam centroid motion, in our model, is governed by the following fields: i) helical quadrupole field, ii) longitudinal magnetic field, iii) electromagnetic fields, and iv) induced image fields.

2.1 Wave equation

Before developing the orbit equations for the beam centroid, we first derive the wave equation for the electromagnetic fields. The electromagnetic fields are represented by a vector potential given by,

$$\mathbf{A} = \mathbf{A}_+(x, y, z)e^{-i\omega t} + \mathbf{A}_-(x, y, z)e^{-i\omega t} + c.c., \tag{1}$$

where $\mathbf{A}_+$ and $\mathbf{A}_-$ are complex amplitudes associated with the right-hand (RH) and left-hand (LH) circularly polarized waves in a cylindrical waveguide. In Eq. (1), ω is the radian frequency and c.c. denotes the complex conjugate.

The wave equation for $\mathbf{A}$ is given by

$$\left(\nabla_\perp^2 + \frac{\partial^2}{\partial z^2} - \frac{1}{c^2}\frac{\partial^2}{\partial t^2}\right)\mathbf{A} = -\frac{4\pi}{c}\mathbf{J}, \tag{2}$$

where $\nabla_\perp^2$ is the transverse Laplacian, and $\mathbf{J}$ is the macroscopic transverse current associated with the beam centroid. Substituting (1) into (2) and operating on the result with $(\omega/2\pi)\int_0^{2\pi/\omega} dt \exp(i\omega t)$, in order to select the correct frequency dependence, yields

$$L(\mathbf{A}_+ + \mathbf{A}_-) = -\frac{4\pi}{c}\int_0^{2\pi/\omega} \frac{dt}{2\pi/\omega} e^{i\omega t}\mathbf{J}, \tag{3}$$

where $L = \nabla_\perp^2 + \partial^2/\partial z^2 + \omega^2/c^2$. To obtain the RH and LH polarized components of the current, we equate the $\hat{\mathbf{e}}_+$ and $\hat{\mathbf{e}}_-$ components of both sides of (3), and find the following wave equation,

$$L(\mathbf{A}_+ + \mathbf{A}_-)\cdot(2\hat{\mathbf{e}}_\mp) = -\frac{4\pi}{c}\int_0^{2\pi/\omega}\frac{dt}{2\pi/\omega}(J_{cx} \mp iJ_{cy})e^{i\omega t}, \tag{4}$$

where $\hat{\mathbf{e}}_\pm = (\hat{\mathbf{e}}_x \pm i\hat{\mathbf{e}}_y)/2$ and $\hat{\mathbf{e}}_x$ and $\hat{\mathbf{e}}_y$ denote unit vectors in the x and y directions.

The current density associated with the beam centroid motion is

$$\mathbf{J}(x, y, z, t) = -|e|\lambda_b\int_{-\infty}^{\infty}dz_0\left(\frac{\partial x_c(z_o, t)}{\partial t}\hat{\mathbf{e}}_x + \frac{\partial y_c(z_o, t)}{\partial t}\hat{\mathbf{e}}_y\right) \times \delta(x - x_c(z_o, t))\delta(y - y_c(z_o, t))\delta(z - z_c(z_o, t)), \tag{5}$$

where $\lambda_b = n_b\pi r_b^2$ is the number of electrons per unit length, n_b is the beam density, r_b is the beam radius, x_c and y_c denote the transverse coordinates of the beam centroid, z_c denotes the axial position of a cross sectional slice of the beam and z_o is the initial position of the slice: $z_c(z_o, t = 0) = z_o$. In the small-signal or linear regime x_c and y_c are proportional to the electromagnetic fields and (5) can be written as

$$\mathbf{J}_c(x, y, z, t) \simeq -|e|\lambda_b\delta(x)\delta(y)\int_{-\infty}^{\infty}dz_o\left(\frac{\partial x_c(z_o, t)}{\partial t}\hat{\mathbf{e}}_x + \frac{\partial y_c(z_o, t)}{\partial t}\hat{\mathbf{e}}_y\right)\delta(z - z_c(z_o, t)), \tag{6}$$

where v_o is the axial beam velocity. Substituting (6) into (4), we obtain

$$L(\mathbf{A}_+ + \mathbf{A}_-)\cdot(2\hat{\mathbf{e}}_\mp) = \frac{4\pi}{c}v\delta(x)\delta(y)\int_0^{2\pi/\omega}\frac{dt}{2\pi/\omega}\int_{-\infty}^{\infty}dz_o \times\left(\frac{\partial x_c(z_o, t)}{\partial t} \mp i\frac{\partial y_c(z_o, t)}{\partial t}\right)\delta(z - z_o - v_o t)e^{i\omega t}, \tag{7}$$

where $v = (|e|/m_o c^2)I_b'\beta_o \simeq I_b[kA]/17\beta_o$ is Budker's parameter, I_b is the beam current and $\beta_o = v_o/c$. Upon carrying out the time integration in (7) we obtain,

$$L(\mathbf{A}_+ + \mathbf{A}_-)\cdot(2\hat{\mathbf{e}}_\mp) = \frac{4\pi}{c}v\delta(x)\delta(y)e^{i(\omega/v_o)z}\int_0^{2\pi v_o/\omega}\frac{dz_o}{2\pi v_o/\omega}\frac{\partial}{\partial z}(x_c \mp iy_c)e^{-i\omega z_o/v_o}, \tag{8}$$

where $x_c(z_o, z) = x_c(z_o, t = (z - z_o)/v_o)$ and $y_c(z_o, z) = y_c(z_o, t = (z - z_o)/v_o)$. Since our model is spatially periodic with period $\omega/2\pi$, the limits on the z_o integral have been changed to 0 to $2\pi/\omega$.

2.2 *Beam centroid orbit*

The configuration of the helical quadrupole and the axial magnetic fields are shown in Figure 1. The total external magnetic field, $\mathbf{B}_{ext}$, consists of the helical quadrupole field and the uniform longitudinal field and is given by $\mathbf{B}_{ext} = (B_{qx}, B_{qy}, B_{zo})$ where

$$B_{qx} = -B_q k_q(x\sin k_q z - y\cos k_q z),$$
$$B_{qy} = B_q k_q(x\cos k_q z + y\sin k_q z), \tag{9a–c}$$
$$B_{zo} = B_o.$$

In Eqs. (9a–c), B_o is the axial magnetic field, B_q is the magnetic field of the quadrupole, $k_q = 2\pi/\lambda_q$ is taken to be positive and λ_q is the period of the quadrupole field. The representation for the quadrupole field in Eqs. (9a,b) is valid near the z axis, i.e., $(x^2 + y^2)^{1/2} \ll \lambda_q/2\pi$.

In addition to the electromagnetic fields given by Eq. (1) and external fields given by Eq. (9), we have induced fields due to the displaced beam. These fields are produced by the image charges and currents on the waveguide wall when the beam is displaced off the z axis. The model assumes that the characteristic length of the axial variation in the beam displacement is much longer than the waveguide radius. For a circular, perfectly conducting waveguide the induced electric and magnetic fields near the z axis are

$$\mathbf{E}_{\text{ind}} = -2\frac{m_o c^2}{|e|}\frac{v}{r_g^2}(x_c\hat{\mathbf{e}}_x + y_c\hat{\mathbf{e}}_y), \tag{10a}$$

$$\mathbf{B}_{\text{ind}} = 2\frac{m_o c^2}{|e|}\frac{v}{r_g^2}\beta_o(y_c\hat{\mathbf{e}}_x - x_c\hat{\mathbf{e}}_y), \tag{10b}$$

where r_g is the waveguide radius and we have additionally assumed that $(x_c^2 + y_c^2)^{1/2} \ll r_g$. The motion of the beam's centroid under the influence of the fields in Eqs. (1), (9) and (10) is in the linear approximation governed by

$$\frac{d^2x_c}{dt^2} + \Omega_o\frac{dy_c}{dt} - v_o k_q\Omega_q(x_c\cos k_q z + y_c\sin k_q z) - v_o^2 k_s^2 x_c = \frac{|e|}{\gamma_o m_o c}\left(\frac{\partial}{\partial t} + v_o\frac{\partial}{\partial z}\right)A_x, \tag{11a}$$

$$\frac{d^2y_c}{dt^2} - \Omega_o\frac{dx_c}{dt} + v_o k_q\Omega_q(y_c\cos k_q z - x_c\sin k_q z) - v_o^2 k_s^2 y_c = \frac{|e|}{\gamma_o m_o c}\left(\frac{\partial}{\partial t} + v_o\frac{\partial}{\partial z}\right)A_y, \tag{11b}$$

where $\Omega_o = |e|B_o/\gamma_o m_o c$ is the relativistic cyclotron frequency associated with the axial field, $\Omega_q = |e|B_q/\gamma_o m_o c$ is the relativistic cyclotron frequency associated with the helical quadrupole field, $\gamma_o = (1 - \beta_0^2)^{-1/2}$ is the relativistic mass factor, $k_s = (2v/[\beta_o^2\gamma_o^3 r_g^2])^{1/2}$, $z = z_o + v_o t$, and A_x, A_y are the x and y components of the vector potential given in Eq. (1). For the purpose here, we will approximate the exact expressions of (1) by the fields on axis,

$$\frac{|e|}{m_o c^2}\mathbf{A}_\pm(x = 0, y = 0, z) = a_\pm e^{ik_\pm z}\hat{\mathbf{e}}_\pm,$$

where $k_\pm$ are the axial wave numbers.

The orbit equations for the beam's centroid can be written in a more convenient form. Setting $\xi = x_c + iy_c$, Eqs. (11a,b) become

$$\left(\frac{\partial^2}{\partial z^2} - iK_o\frac{\partial}{\partial z} - k_s^2\right)\xi - K_q k_q e^{ik_q z}\xi^* = F \tag{12}$$

where $K_o = \Omega_o/v_o$, $K_q = \Omega_q/v_o$, and

$$F = \frac{1}{\beta_o\gamma_o}[-i(k_+^* - \omega/v_o)a_+^* e^{-i(k_+^* - \omega/v_o)z}e^{-i\omega z_o/v_o} + i(k_- - \omega/v_o)a_- e^{i(k_- - \omega/v_o)z}e^{i\omega z_o/v_o}]. \tag{13}$$

It is convenient at this point to introduce a transformation from the quantity ξ to $\hat{\xi}$

$$\xi = \hat{\xi} e^{+ik_q z/2}. \tag{14}$$

Substituting Eq. (14) into Eq. (13) transforms the beam's centroid equation into

$$\left[\frac{\partial^2}{\partial z^2} - iK_1 \frac{\partial}{\partial z} + K_2^2\right]\hat{\xi} - K_3^2 \hat{\xi}^* = G, \tag{15}$$

where

$$K_1 = K_o - k_q,\ K_2^2 = (K_o - k_q/2)k_q/2 - k_s^2,\ K_3^2 = K_q k_q \quad \text{and} \quad G = F \exp(-ik_q z/2).$$

Equation (15) can be written in the form

$$\left[\frac{\partial^4}{\partial z^4} + (2K_2^2 + K_1^2)\frac{\partial^2}{\partial z^2} + (K_2^4 - K_3^4)\right]\hat{\xi} = H, \tag{16a}$$

where

$$\begin{aligned} H &= \left[\frac{\partial^4}{\partial z^4} + iK_1 \frac{\partial^2}{\partial z^2} + K_2^2\right]G + K_3^2 G^* \\ &= e^{-ik_q z/2}\left[\frac{\partial^2}{\partial z^2} + i(K_1 - k_q)\frac{\partial}{\partial z} + ((K_1 - k_q/2)k_q/2 + K_2^2)\right]F + K_3^2 F^* e^{ik_q z/2}. \end{aligned} \tag{16b}$$

Substituting Eq. (13) into Eq. (16b) yields

$$\begin{aligned} H = {} & \frac{i}{\beta_o \gamma_o}[(K_+^* - k_q/2)D_+^* a_+^* e^{-iK_+^* z} - (K_-^* + k_q/2)K_3^2 a_-^* e^{-iK_-^* z}]e^{-i\omega z_o/v_o} \\ & - \frac{i}{\beta_o \gamma_o}[(K_- - k_q/2)D_- a_- e^{iK_- z} - (K_+ + k_q/2)K_3^2 a_+ e^{iK_+ z}]e^{i\omega z_o/v_o}, \end{aligned} \tag{17}$$

where $K_\pm = k_\pm - \omega/v_o \pm k_q/2$ and $D_\pm = K_\pm^2 \mp K_1 K_\pm - K_2^2$. The particular solution to Eq. (16a) is

$$\hat{\xi} = (\alpha_+^* a_+^* e^{-iK_+^* z} + \beta_-^* a_-^* e^{-iK_-^* z})e^{-i\omega z_o/v_o} + (\alpha_- a_- e^{iK_- z} + \beta_+ a_+ e^{iK_+ z})e^{i\omega z_o/v_o}, \tag{18a}$$

where

$$\begin{aligned} \alpha_\pm &= -\frac{i}{\beta_o \gamma_o} D_\pm (k_\pm - \omega/v_o)/R_\pm, \\ \beta_\pm &= -K_3^2 \alpha_\pm / D_\pm, \\ R_\pm &= K_\pm^4 - (2K_2^2 + K_1^2)K_\pm^2 + K_2^4 - K_3^4 \\ &= (K_\pm^2 - (d_1^2 + d_2^2))(K_\pm^2 - (d_1^2 - d_2^2)), \\ d_1^2 &= K_2^2 + K_1^2/2, \\ d_2^2 &= ((K_2^2 + K_1^2/2)^2 - (K_2^4 - K_3^4))^{1/2}. \end{aligned} \tag{18b–f}$$

For given values of ω, k_+ and k_- (to be determined by solving the dispersion relation) the electron beam centroid motion is given by Eqs. (14) and (18). The wave number of the beam centroid oscillation is ω/v_o.

Substituting Eq. (18) together with Eq. (14) into Eq. (8), the right-hand side of the wave equation becomes

$$-\frac{4\pi}{c}\int_0^{2\pi/\omega}\frac{dt}{2\pi/\omega}(J_{cx}\mp iJ_{cy})e^{i\omega t} = 4\pi i v\beta_o\frac{m_oc^2}{|e|}\delta(x)\delta(y)e^{i\omega z/v_o}$$
$$\times[(K_\pm\mp k_q/2)\alpha_\pm a_\pm e^{i(K_\pm\mp k_q/2)z}$$
$$+(K_\mp\mp k_q/2)\beta_\mp a_\mp e^{i(K_\mp\mp k_q/2)z}]. \tag{19}$$

2.3 *Dispersion relation*

To obtain the dispersion relation the coupled differential equation must be solved, subject to the boundary conditions on the waveguide. To this end, we assume that the electron beam propagates within a perfectly conducting cylindrical waveguide of radius r_g. In general, the complex amplitude for the right- and left-hand circularly polarized TE waves are written as,

$$\mathbf{A}_\pm(r,\theta,z)e^{-i\omega t} = \sum_{n,m} b_{\pm nm}[J_{n-1}(\mu_{nm}r)\hat{\mathbf{e}}_\pm + J_{n+1}(\mu_{nm}r)e^{\pm i2\theta}\hat{\mathbf{e}}_\mp]$$
$$\times\exp[i(k_{\pm nm}z\pm(n-1)\theta-\omega t)], \tag{20}$$

where J_n is the nth order Bessel function, $b_{\pm nm}$ are complex constants, μ_{nm} are real constants determined by the boundary conditions and $n = 1, 2, 3, \ldots$ and $m = 1, 2, 3, \ldots$ are waveguide mode indices.

The boundary condition is such that the tangential component of the electric field vanishes on the waveguide surface, $r = r_g$. At $r = r_g$ we have $\mathbf{E}\cdot\hat{\mathbf{e}}_\theta = 0$, where $\mathbf{E}$ is the total electric field and $\hat{\mathbf{e}}_\theta = -i\exp(-i\theta)\hat{\mathbf{e}}_+ + i\exp(-i\theta)\hat{\mathbf{e}}_-$ is the unit vector in the azimuthal direction. Applying the boundary condition at $r = r_g$, we find the condition $J_n'(\mu_{nm}r_g) = 0$, so that $\mu_{nm}r_g$ equals the mth positive zero of J_n'.

Since $\mathbf{A}$ is driven by an effective transverse line current, we expect TE_{1m} modes will be excited. Substituting the TE_{1m} mode representation into the left-hand side of Eq. (4), we obtain two sets of coupled equations.

$$\sum_m e^{ik_{\pm 1m}z}\left(\frac{\omega^2}{c^2}-k_{\pm 1m}^2-\mu_{1m}^2\right)J_o(\mu_{1m}r)b_{\pm 1m}$$
$$+\sum_m e^{ik_{\mp 1m}z}\left(\frac{\omega^2}{c^2}-k_{\mp 1m}^2-\mu_{1m}^2\right)J_2(\mu_{1m}r)e^{\mp i2\theta}b_{\mp 1m}$$
$$=-\frac{4\pi}{c}\frac{|e|}{m_oc^2}\int_0^{2\pi/\omega}\frac{dt}{2\pi/\omega}e^{i\omega t}(J_x\mp iJ_y)\Big|_{r=0}. \tag{21}$$

Operating on Eq. (21) by both $\int_0^{2\pi} d\theta \int_0^{r_g} J_o(\mu_{1m} r) r\, dr$ and $\int_0^{2\pi} d\theta e^{\mp i2\theta} \int_0^{r_g} J_2(\mu_{1m} r) r\, dr$ and solving for $b_{\pm 1m}$, we find that

$$\left(\frac{\omega^2}{c^2} - k_{\pm 1m}^2 - \mu_{1m}^2\right) b_{\pm 1m} e^{ik_{\pm 1m} z} = -\frac{2}{c} \frac{1}{I_{1m}} \frac{|e|}{m_o c^2} \int_0^{2\pi} d\theta \int_0^{r_g} r\, dr \int_0^{2\pi/\omega} \frac{dt}{2\pi/\omega} e^{i\omega t}$$
$$\times [J_o(\mu_{1m} r)(J_x \mp iJ_y)|_{r=0} + J_2(\mu_{1m} r)(J_x \pm iJ_y)|_{r=0} e^{\mp i2\theta}], \quad (22)$$

where $I_{1m} = \int_0^{r_g} [J_0^2(\mu_{1m} r) + J_2^2(\mu_{1m} r)] r\, dr = (\mu_{1m}^2 r_g^2 - 1)\mu_{1m}^{-2} J_1^2(\mu_{1m} r_g)$.

The dispersion relation greatly simplifies when only one waveguide mode, say the TE_{11}, takes part in the interaction, i.e., $n = 1$, $m = 1$, $a_\pm = b_{\pm 11}$, $k_\pm = k_{\pm 11}$.

Substituting Eq. (19) into the right-hand-side of Eq. (22), we obtain

$$\left[\left(\frac{\omega^2}{c^2} - k_{\pm 1m}^2 - \mu_{1m}^2\right) R_\pm - k_b^2 \left(k_\pm - \frac{\omega}{v_o}\right)^2 D_\pm\right] b_{\pm 11} e^{ik_\pm z}$$
$$= -k_b^2 K_3^2 \left(k_\pm - \frac{\omega}{v_o}\right)\left(k_\mp - \frac{\omega}{v_o} \mp k_q\right) b_{\mp 11} e^{i(k_\mp \mp k_q) z}, \quad (22)$$

where $k_b^2 = 2\nu/\gamma_o I_{11} = 2\nu\mu_{11}^2/(\gamma_o(\mu_{11}^2 r_g^2 - 1)J_1^2(\mu_{11} r_g))$. The RH and LH circularly polarized waves are simultaneously excited only when $k_+ = k_- - k_q$. Eliminating $b_{\pm 11}$, the dispersion relation coupling the RH and LH circularly polarized waves becomes

$$\left[R - \frac{k_b^2 (k - \omega/v_o + k_q)^2 D_-}{\omega^2/c^2 - (k + k_q)^2 - \mu_{11}^2}\right]\left[R - \frac{k_b^2 (k - \omega/v_o)^2 D_+}{\omega^2/c^2 - k^2 - \mu_{11}^2}\right]$$
$$= k_b^4 K_3^4 \left(\frac{(k - \omega/v_o)^2}{\omega^2/c^2 - k^2 - \mu_{11}^2}\right)\left(\frac{(k - \omega/v_o + k_q)^2}{\omega^2/c^2 - (k + k_q)^2 - \mu_{11}^2}\right), \quad (24)$$

where $k = k_+$, $k_- = k + k_q$, $K = K_\pm = k - \omega/v_o + k_q/2$, $D_\pm = K^2 \mp K_1 K - K_2^2$ and $R = R_\pm = D_+ D_- - K_3^4 = K^4 - (2K_2^2 + K_1^2)K^2 + K_2^4 - K_3^4$. Equation (24) can be put into the form

$$\left[D_+ - \frac{k_b^2 (k - \omega/v_o + k_q)^2}{\omega^2/c^2 - (k + k_q)^2 - \mu_{11}^2}\right]\left[D_- - \frac{k_b^2 (k - \omega/v_o)^2}{\omega^2/c^2 - k^2 - \mu_{11}^2}\right] - K_3^4 = 0, \quad (25a)$$

and/or

$$R = 0. \quad (25b)$$

Equation (25a) agrees with the dispersion relation in Ref. [3] with the vertical field set to zero. Equation (25b) is the dispersion relation of the hybrid cyclotron and quadrupole modes with image fields in a waveguide in the absence of electromagnetic fields.

The dispersion relation possesses the following symmetry:

$$(k, k_q, B_o) \Leftrightarrow (k - k_q, -k_q, -B_o).$$

Utilizing this symmetry condition, the discussions in Section 3 can also be applied to helical quadrupoles of the opposite helicity. In this paper, the value for k_q is

always assumed to be positive. The polarization of the waveguide mode associated with the three-wave unstable wave number k is determined by the polarization of the waveguide mode that intersects the unstable beam modes.

The modes taking part in the interaction can be conveniently classified by setting the beam current equal to zero. The dispersion relation, for zero beam current, reduces to

$$[k^2 - \omega^2/c^2 + \mu_{11}^2][(k + k_q)^2 - \omega^2/c^2 + \mu_{11}^2]$$
$$\times [(k - \omega/v_o + k_q/2)^2 - (d_1^2 + d_2^2)][(k - \omega/v_o + k_q/2)^2 - (d_1^2 - d_2^2)] \simeq 0, \quad (26)$$

where

$$d_1^2 \simeq \tfrac{1}{2}(K_o(K_o - k_q) + k_q^2/2),$$
$$d_2^2 \simeq \tfrac{1}{2}(K_o^2(K_o - k_q)^2 + 4K_q^2 k_q^2)^{1/2}.$$

The first and second bracketed terms on the left-hand side of Eq. (26) represent the LH and RH circularly polarized transverse electric waveguide modes, while the third and fourth terms, R, are hybrid cyclotron and quadrupole modes.

The three-wave instabilities are associated with the intersection of the beam lines

$$(k - \omega/v_o + k_q/2)^2 - (d_1^2 - d_2^2) = 0, \quad (27)$$

with the waveguide modes. Let us define

$$U_\pm \equiv \left(\frac{\omega}{v_o} - k\right) - \left(\frac{k_q}{2} \pm \sqrt{d_1^2 - d_2^2}\right) = 0 \quad (28)$$

to be the beam lines that can lead to instabilities, where $d_1^2 - d_2^2 > 0$; and

$$S_\pm \equiv \left(\frac{\omega}{v_o} - k\right) - \left(\frac{k_q}{2} \pm \sqrt{d_1^2 + d_2^2}\right) = 0 \quad (29)$$

to be the beam lines that do not lead to instabilities. Note that for $K_o < k_q/2$ only U_+ is unstable for $\omega > 0$, where as for $K_o > k_q/2$ the unstable mode is U_-.

The approximate factorization of the beam lines, in the limit of $I_b = 0$ and $K_q \to 0$, provides simplified understanding of the nature of the three-wave instability in different operating regimes:

a) For $K_o < 0$,

$$U_+ \simeq \chi - k_q, \quad U_- \simeq \chi, \quad S_+ \simeq \chi + K_o - k_q, \quad S_- \simeq \chi - K_o; \quad (30a)$$

b) for $0 < K_o < k_q/2$,

$$U_+ \simeq \chi + K_o - k_q, \quad U_- \simeq \chi - K_o, \quad S_+ \simeq \chi - k_q, \quad S_- \simeq \chi; \quad (30b)$$

c) for $k_q/2 < K_o < k_q$,

$$U_+ \simeq \chi - K_o, \quad U_- \simeq \chi + K_o - k_q, \quad S_+ \simeq \chi - k_q, \quad S_- \simeq \chi; \quad (30c)$$

d) for $k_q < K_o$,

$$U_+ \simeq \chi - k_q, \quad U_- \simeq \chi, \quad S_+ \simeq \chi - K_o, \quad S_- \simeq \chi + K_o - k_q, \quad (30d)$$

where $\chi = \omega/v_o - k$.

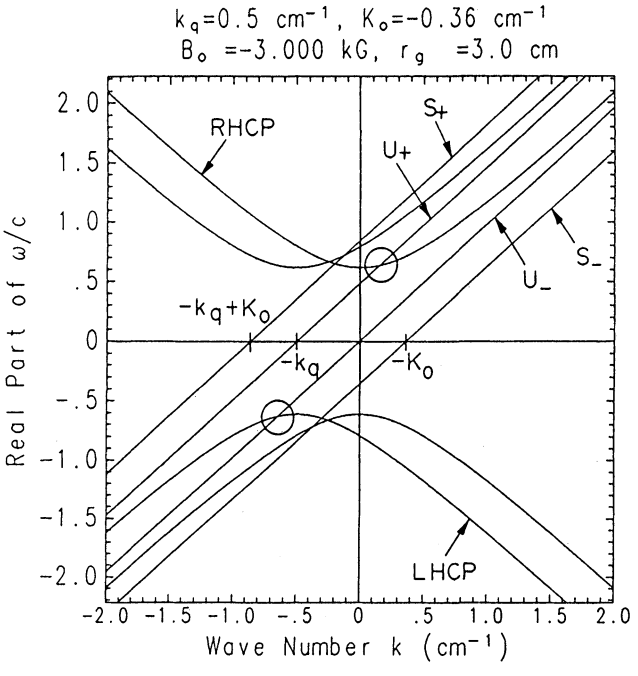

(a)

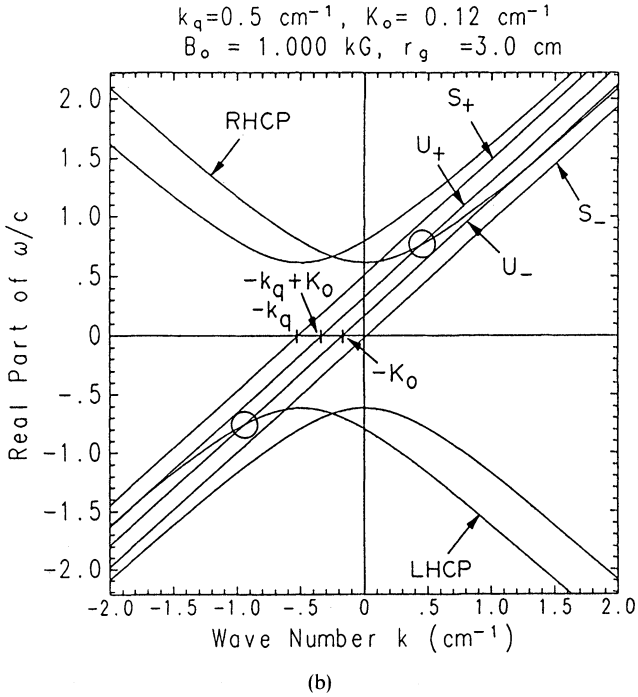

(b)

FIGURE 2 The dispersion diagram in the limit of zero beam current for a) $K_o < 0$, b) $0 < K_o < k_q/2$, c) $k_q/2 < K_o < k_q$ and d) $k_q < K_o$. The beam lines that can lead to instabilities are labeled by U_+ and U_-. The intersections where the instabilities occur are circled.

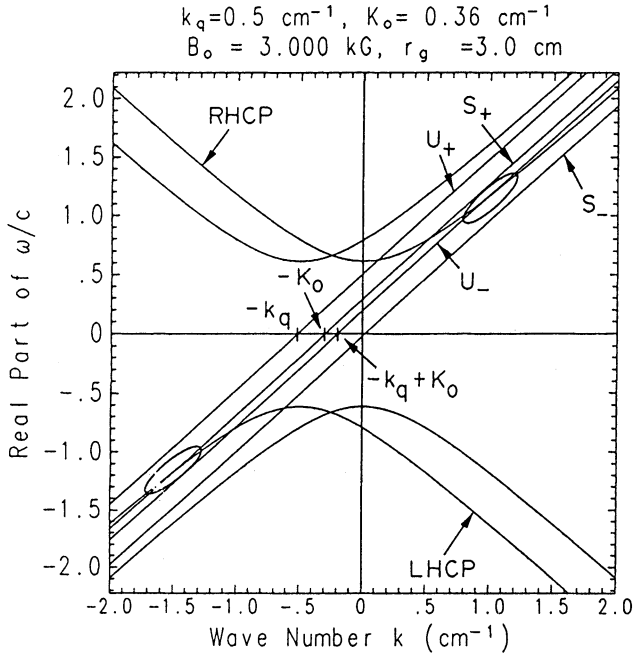

(c)

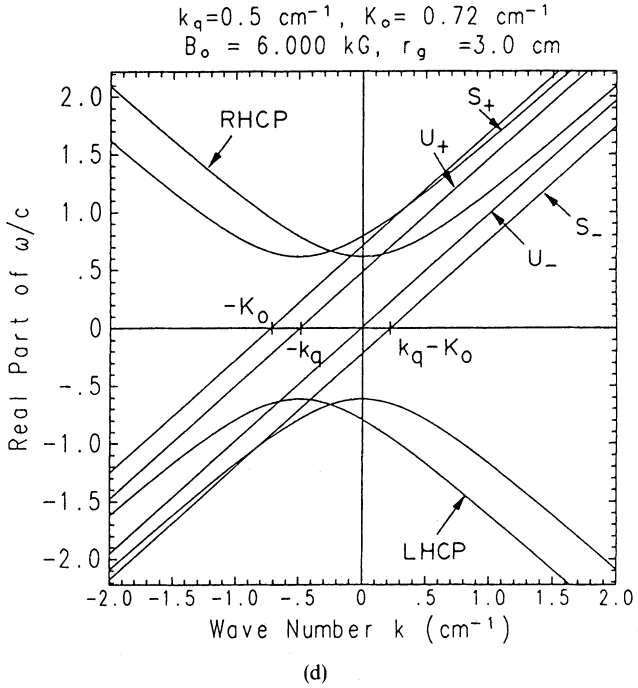

(d)

FIGURE 2 (*Continued*)

In this notation, the simplified dispersion relation, with zero beam current, reduces to

$$[k^2 - \omega^2/c^2 + \mu_{11}^2][(k + k_q)^2 - \omega^2/c^2 + \mu_{11}^2]U_+U_-S_+S_- \simeq 0, \tag{31}$$

where in all cases,

$$U_+U_-S_+S_- \simeq \chi(\chi - k_q)(\chi - K_o)(\chi + K_o - k_q). \tag{32}$$

To illustrate the simplified dispersion diagram, Figures 2a–d show plots of the waveguide modes and the stable and unstable beam lines for cases a–d outlined above. The three-wave instability can occur for situations illustrated by Figures 2a–c, and the intersections where instability occurs are circled. In Figure 2d, the beam line U_- does not intersect the RHCP waveguide mode. Thus, Figure 2d represents three-wave stable operation.

3. STABILITY REGIMES AND ANALYTICAL EXPRESSIONS FOR GROWTH RATES

The dispersion relation, Eq. (25a), contains i) a region of orbital instability (in the absence of the electromagnetic waves), ii) regions of three-wave instability, and iii) regions of stability. In this section, we will obtain the conditions delineating the various regimes and find analytical expressions for the maximum growth rate in each of the three-wave unstable regions. The various stability regimes can be delineated as functions of k_q and K_o for given values of γ_o, r_g and B_qk_q. The boundaries separating the different regimes are obtained in the limit of zero beam current. Figure 3 is a stability diagram for $\gamma_o = 5$, $r_g = 3$ cm and quadrupole gradient $B_qk_q = 200$ G/cm.

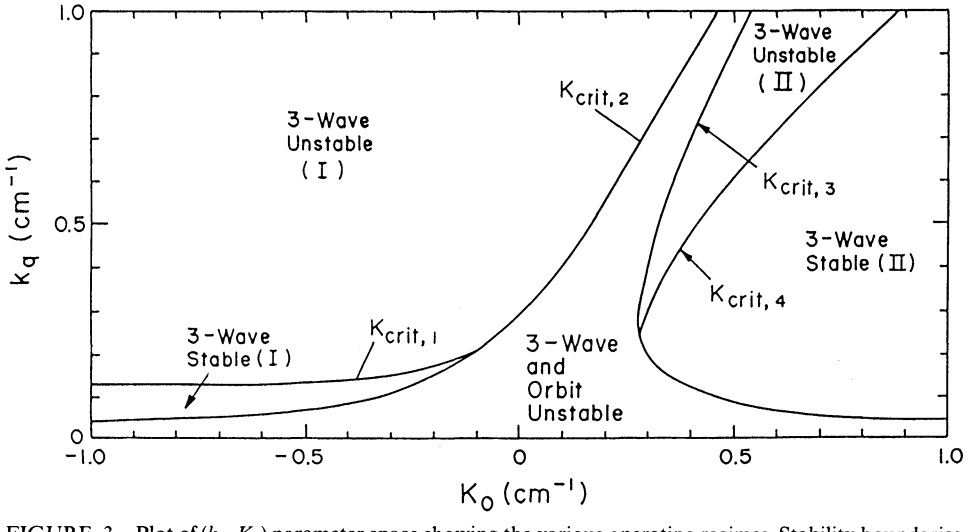

FIGURE 3 Plot of (k_q, K_o) parameter space showing the various operating regimes. Stability boundaries are calculated for parameters of Table I.

3.1 *Orbit-unstable regime*

The expression $R = 0$ (Eq. 25b) is the dispersion relation for the particle dynamics in the presence of stellarator windings with an axial magnetic field. This expression is in agreement with Eq. (10) of Ref. 2 in the limit of perfectly conducting walls. The electron beam in this configuration can be unstable when $(d_1^2 - d_2^2) \leq 0$. The unstable values of K_o are

$$K_{\text{crit},2} \equiv \frac{k_q}{2} - 2K_q \leq K_o \leq K_{\text{crit},3} \equiv \frac{k_q}{2} + 2K_q, \tag{33}$$

where $K_q = \Omega_q/v_o$, $\Omega_q = |e|B_q/\gamma_o m_o c$, $K_o = \Omega_o/v_o$ and $\Omega_o = |e|B_o/\gamma_o m_o c$. The curves in (k_q, K_p) parameter space given by $K_o = K_{\text{crit},2}$ and $K_o = K_{\text{crit},3}$ are the left and right boundaries of the orbit-unstable region shown in Figure 3.

Equation (33) is in agreement with the stability condition of Ref. [1] in the limit of straight cylindrical geometry and zero beam current. It is interesting to note that this condition is also in agreement with the condition for beam envelope stability in the limit of zero space charge.[13]

3.2 *Three-wave unstable regimes*

The three-wave instability will occur when, for example, the RHCP waveguide mode intersects, in the (ω, k) plane, the appropriate beam mode given by Eq. (28). For $k_q > 0$, the instability for the RHCP waveguide mode occurs with $\omega > 0$. Identical three-wave instability growth rates occur for the LHCP waveguide mode with $\omega < 0$.

For $K_o < K_{\text{crit},2}$, the three-wave instability occurs (Region I) when the RHCP waveguide mode intersects the beam line U_+ given in Eq. (28). This corresponds to the situation in Figures 2a and 2b. For $K_{\text{crit},3} < K_o < k_q$, the three-wave instability occurs (Region II) when the RHCP waveguide mode intersects the beam line U_- given in Eq. (28). This corresponds to the situation in Figure 2c.

3.3 *Three-wave stable regime for* $K_o < K_{\text{crit},2}$

Stability is achieved when the waveguide cutoff frequency $\mu_{11}c$ is sufficiently large so that intersection with either of the beam lines, defined by Eq. (28), cannot be achieved. This is stable regime I in Figure 3. The condition in terms of the waveguide mode cutoff is

$$q\mu_{11} \geq k_q + 2(d_1^2 - d_2^2)^{1/2}, \tag{34}$$

where

$$q = \left(\frac{4}{\gamma_o^2 - 2}\right)^{1/2}.$$

Based on Eq. (34), the region of

$$k_q > q\mu_{11} \quad \text{and} \quad K_o < K_{\text{crit},2} \tag{35}$$

is always three-wave unstable. If the inequality in (34) can be satisfied, we can solve for the explicit values of K_o for the three-wave stable regime.

For $k_q < q\mu_{11}$ and $K_o < K_{\text{crit},2}$, condition for stability in terms of the variable K_o is

$$2fK_o(K_o - k_q) + f^2 - 4K_q k_q < 0, \tag{36}$$

where

$$f = q\mu_{11}(k_q - q\mu_{11}/2). \tag{37}$$

Defining

$$\zeta = k_q^2\left(1 + \frac{8K_q^2}{f}\right) - 2f, \tag{38}$$

we solve for K_o with $k_q < q\mu_{11}$, and find four situations:

i) for $f > 0$ and $\zeta > 0$, the stable range of K_o is given by

$$K_{\text{crit},1} \equiv \frac{k_q}{2} - \frac{\zeta^{1/2}}{2} < K_o < K_{\text{crit},2}, \tag{39a}$$

ii) for $f < 0$ and $\zeta > 0$, the stable values of K_o are

$$K_o < K_{\text{crit},1} \equiv \text{smaller of}\left(\frac{k_q}{2} - \frac{\zeta^{1/2}}{2}, K_{\text{crit},2}\right), \tag{39b}$$

iii) for $f > 0$ and $\zeta < 0$, all values of

$$K_o < K_{\text{crit},2} \tag{39c}$$

are unstable,

iv) for $f < 0$ and $\zeta < 0$, all values of

$$K_o < K_{\text{crit},2} \tag{39d}$$

are stable. The curve $K_o = K_{\text{crit},1}$ denotes the upper boundary of stable region I in Figure 3.

3.4 Three-wave stable regime for $K_o > K_{\text{crit},3}$

The three-wave interaction is also stable when the RHCP waveguide mode does not intersect the beam mode U_- associated with Eq. (28) and $K_o > K_{\text{crit},3}$. This is stable region II. This occurs when

$$q\mu_{11} \geq k_q - 2(d_1^2 - d_2^2)^{1/2}. \tag{40}$$

The three-wave interaction is stable for

$$k_q < q\mu_{11} \quad \text{and} \quad K_o > K_{\text{crit},3}. \tag{41}$$

For $k_q > q\mu_{11}$ and $K_o > K_{\text{crit},3}$, the values of K_o that are three-wave stable are

$$K_o > K_{\text{crit},4} \equiv \frac{k_q}{2} + \frac{\zeta^{1/2}}{2}. \tag{42}$$

The curve $K_o = K_{\text{crit},4}$ denotes the upper boundary of stable region II in Figure 3.

In this regime, one can show that $f > 0$ and $\zeta > 0$. For $K_0 > K_{\text{crit},3}$ in the limit

$\gamma \gg 1$ the stability condition is approximately

$$K_0 > \frac{k_q}{2} + \frac{1}{2}\left[\left(k_q - \frac{2\mu_{11}}{\gamma}\right)^2 + \frac{4\gamma k_q^2 K_q^2}{\mu_{11}(k_q - \mu_{11}/\gamma)}\right]^{1/2}. \tag{43}$$

Equation (43) gives a lower limit on K_0 for given values of γ, k_q, K_q and r_g such that as the beam energy increases, greater values of $B_0 > 0$ are required for stability. Note that for small quadrupole gradient, $K_q \ll (k_q\mu_{11}/4\gamma)^{1/2}$, Eq. (43) reduces to $K_0 > k_q - \mu_{11}/\gamma_0$.[11]

The stability diagram, Figure 3, assumes that the quadrupole gradient is a constant, and (k_q, K_o) are allowed to vary. The horizontal separation of the boundaries for the orbital unstable region is $4K_q$. Since the stability boundaries are obtained in the limit of zero beam current, the area of the actual stable regions will shrink slightly as the value of the current is increased.

3.5 *Analytical expressions for the growth rates*

In the three-wave unstable regimes, we can obtain analytical expressions for the peak growth rates. The dispersion relation (25a) for the coupled RHCP and LHCP wave can be rewritten as

$$(\omega^2 - \omega_1^2)((\omega - \omega_2)^2 - \Delta\omega_1^2)((\omega - \omega_2)^2 - \Delta\omega_2^2)(\omega^2 - \omega_3^2) = \bar{\sigma}, \tag{44}$$

where

$$\bar{\sigma} = k_b^2 v_o^2 c^2[(\omega - v_o k)^2(\omega^2 - \omega_3^2)D_+ + (\omega - v_o(k + k_q))^2(\omega^2 - \omega_1^2)D_-],$$

$\omega_1 = \sqrt{k^2 + \mu_{11}^2}c$, $\omega_2 = v_o(k + k_q/2)$, $\omega_3 = \sqrt{(k + k_q)^2 + \mu_{11}^2}c$, $\Delta\omega_1^2 = v_o^2(d_1^2 + d_2^2)$, and $\Delta\omega_2^2 = v_0^2(d_1^2 - d_2^2)$. Based on the numerical results of the full dispersion relation in Eq. (25a), instability occurs at the intersection of the RHCP waveguide mode and one of the two modes of Eq. (28) for $k_q > 0$ and $\omega > 0$. Defining $\omega = \omega_1 + \delta\omega$ and $\sigma = \bar{\sigma}|_{\omega=\omega_1}$, the dispersion relation reduces to

$$(\omega^2 - \omega_1^2)((\omega - \omega_2)^2 - \Delta\omega_1^2)((\omega - \omega_2)^2 - \Delta\omega_2^2) = \sigma, \tag{45}$$

where $\sigma = k_b^2 v_o^2 c^2(\omega_1 - v_o k)^2 D_+|_{\omega=\omega_2\pm\Delta\omega_2}$, $D_+|_{\omega=\omega_2\pm\Delta\omega_2} = (\Delta\omega_2/c)^2 \pm K_1(\Delta\omega_2/c) - K_2^2$ and the top and bottom signs in D_+ refer to the three-wave unstable regions I and II respectively. Equation (45) is the dispersion relation when the RHCP and the LHCP waveguide modes are not simultaneously excited.

The instability region I in Figure 3 is the result of the waveguide mode intersecting the upper mode (the beam line with larger ω for the same k) given in Eq. (28). The condition for this interaction is $\omega_1 = \omega_2 + \Delta\omega_2$. The unstable wavenumber k satisfies $(1 - \beta_o^2)k^2 + f_b k + f_c = 0$, where $f_b = -\beta_o(\beta_o k_q + 2\Delta\omega_2/c)$, and $f_c = \mu_{11}^2 - (\beta_o k_q/2 + \Delta\omega_2/c)^2$. In the limit of $(1 - \beta_0^2) \ll f_b^2/(4f_c)$, the unstable wavenumber is approximately $k \simeq -f_c/f_b$. We will assume $\Delta\omega_1 - \Delta\omega_2 \gg \delta\omega$. The dispersion relation is given approximately by

$$\left(\frac{\delta\omega}{c} + 2\frac{\Delta\omega_2}{c}\right)\left(\frac{\delta\omega}{c}\right)^2 = -\frac{\sigma/c^3}{2\omega_1}\frac{1}{(\Delta\omega_1^2 - \Delta\omega_2^2)}. \tag{46}$$

For simplicity, we will assume the temporal growth rate is much smaller than the separation of the beam modes, i.e., $\delta\omega \ll 2\Delta\omega_2$. With this assumption, we obtain a simple expression for the dispersion relation,

$$\left(\frac{\delta\omega}{c}\right)^2 \simeq -\frac{\sigma/c^2}{4\omega_1\Delta\omega_2}\frac{1}{(\Delta\omega_1^2 - \Delta\omega_2^2)}. \tag{47}$$

For values of K_o in the unstable region I, i.e., $K_o < K_{\text{crit},2}$, the values of σ are positive, and Eq. (47) gives the temporal growth rate.

When the RHCP waveguide mode intersects both modes given by Eq. (28) with $k_q > 0$, $\omega > 0$ and $K_o > K_{\text{crit},3}$, the instability occurs only at the intersection of the RHCP wave mode and the lower beam mode. The condition for this interaction is $\omega_1 = \omega_2 - \Delta\omega_2$. In the limit of $(1 - \beta_0^2) \ll f_d^2/(4f_e)$, the unstable wavenumber is approximately $k \simeq -f_e/f_d$, where

$$f_d = -\beta_o(\beta_o k_q - 2\Delta\omega_2/c) \quad \text{and} \quad f_e = \mu_{11}^2 - (\beta_o k_q/2 - \Delta\omega_2/c)^2.$$

This gives the instability regime II in Figure 3. Still assuming $\Delta\omega_1 - \Delta\omega_2 \gg \delta\omega$, the dispersion relation becomes

$$\left(\frac{\delta\omega}{c} - 2\frac{\Delta\omega_2}{c}\right)\left(\frac{\delta\omega}{c}\right)^2 = -\frac{\sigma/c^3}{2\omega_1}\frac{1}{(\Delta\omega_1^2 - \Delta\omega_2^2)}. \tag{48}$$

Here again, we assume $2\Delta\omega_2 \gg \delta\omega$ and the dispersion relation reduces to

$$\left(\frac{\delta\omega}{c}\right)^2 \simeq \frac{\sigma/c^2}{4\omega_1\Delta\omega_2}\frac{1}{(\Delta\omega_1^2 - \Delta\omega_2^2)}. \tag{49}$$

For $K_{\text{crit},3} < K_o < k_q$, the quantity σ is negative, and Eq. (49) gives the temporal growth rate in region II of Figure 3. The analytical expressions Eqs. (47) and (49) show that the temporal growth rate $\Gamma = \text{Im}(\delta\omega)$ scales approximately as the square root of the beam current, i.e., $\Gamma/c \propto I_b^{1/2}$.

4. NUMERICAL RESULTS

The full dispersion relation, Eq. (25a), is solved numerically to: i) obtain the growth rates and group velocities, ii) verify the various operating regimes and the analytical expressions for the temporal growth rates, and iii) show the scaling of the growth rate with respect to the various parameters. The numerical studies center around the parameters shown in Table 1. With the quadrupole wave number k_q chosen to be $0.5\ \text{cm}^{-1}$ ($\lambda_q = 12.57$ cm), we may demonstrate each of the different operating regimes by varying the axial magnetic field, B_o, except in one of the stable regimes, where we take $k_q = 0.1\ \text{cm}^{-1}$.

Figure 3 is a plot of the various operating regimes in the parameter space of k_q as a function of K_o for $\gamma_o = 5$, $B_q k_q = 200$ G/cm and $r_g = 3$ cm as in Table I.

TABLE I

Parameters Used in Section 4.

Quadrupole gradient, $B_q k_q$	200 G/cm
Beam energy (γ_o)	5
Beam current, I_b	1.10 kA
Drift-tube radius, r_g	3 cm
Calculated parameters	
TE_{11} cut-off frequency/c, μ_{11}	0.614 cm^{-1}
$q\mu_{11}$	0.256 cm^{-1}
$K_q k_q$	0.024 cm^{-2}
$\beta_o = v_o/c$	0.9793
For helical quadrupole wavelength, λ_q =	12.57 cm
Wave number, k_q	0.5 cm^{-1}
K_q	0.048 cm^{-1}
$K_{crit,2}$ (B_o = 1.32 kG)	0.154 cm^{-1}
$K_{crit,3}$ (B_o = 2.95 kG)	0.346 cm^{-1}
$K_{crit,4}$ (B_o = 3.52 kG)	0.413 cm^{-1}

4.1 Numerical results from full dispersion relation

The dispersion diagram with current $I_b = 1$ kA for the five different regimes are shown in Figure 4:

a) $B_o = -1.0$ kG ($K_o = -0.12\ cm^{-1}$) and $k_q = 0.5\ cm^{-1}$ in the three-wave unstable region I,

b) $B_o = 2.15$ kG ($K_o = 0.26\ cm^{-1}$) and $k_q = 0.5\ cm^{-1}$ in the orbit-unstable regime,

c) $B_o = 3.5$ kG ($K_o = 0.42\ cm^{-1}$) and $k_q = 0.5\ cm^{-1}$ in the three-wave unstable region II,

d) $B_o = 5.0$ kG ($K_o = 0.60\ cm^{-1}$) and $k_q = 0.5\ cm^{-1}$ in the three-wave stable regime,

e) $B_o = -5.0$ kG ($K_o = -0.60\ cm^{-1}$) and $k_q = 0.1\ cm^{-1}$ in the three-wave stable regime.

The intersections where electromagnetic instability occurs are circled in Figures 4a and 4c. In Figure 4b, the center beam line is unstable along its entire length.

Plots of the temporal growth rate as a function of wave number k are given in Figures 5–7 for each of the different regimes with current $I_b = 1$ kA. Figure 5 shows the temporal growth rates in region I, for $B_o = -1.0$ kG ($K_o = -0.12\ cm^{-1}$), $B_o = 0$, $B_o = 1.0$ kG ($K_o = 0.12\ cm^{-1}$), and $B_o = 1.3$ kG ($K_o = 0.156\ cm^{-1}$). Only the growth rates associated with $\mathrm{Re}(\omega) > 0$ are plotted; these are associated with RHCP waves. The growth rates associated with $\mathrm{Re}(\omega) < 0$ are identical and the wavenumber associated with the instability is at $-(k + k_q)$. The growth rate and the range of unstable values of k increase as K_o approaches the orbit unstable value of $K_{crit,2} = 0.154\ cm^{-1}$.

Figure 6 shows temporal growth rates in the three-wave unstable region II, for $B_o = 2.95$ kG ($K_o = 0.35\ cm^{-1}$), $B_o = 3.0$ kG ($K_o = 0.36\ cm^{-1}$), $B_o = 3.25$ kG

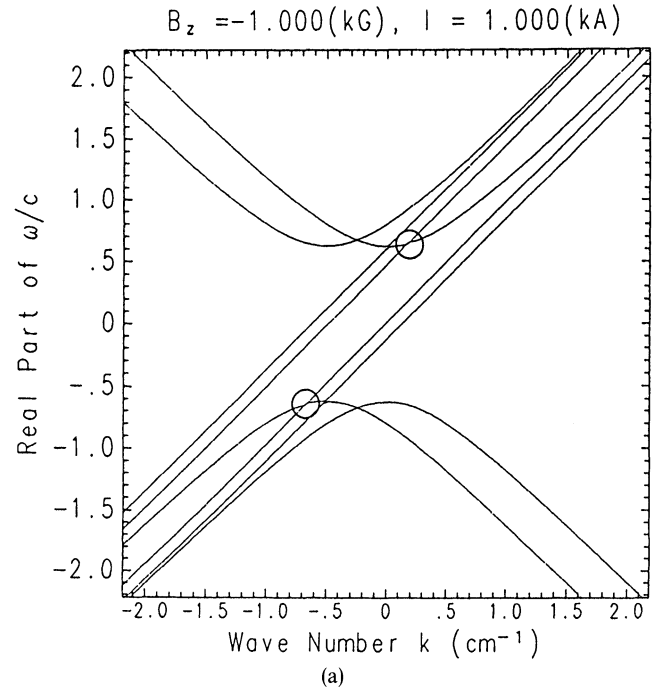

(a)

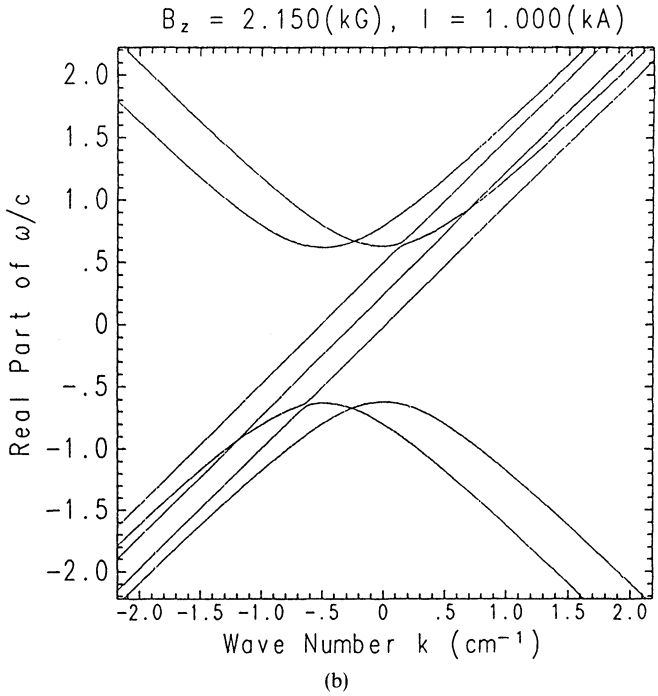

(b)

FIGURE 4 Dispersion diagram for parameters in Table I with: a) $B_o = -1.0$ kG ($K_o = -0.12\ \text{cm}^{-1}$) and $k_q = 0.5\ \text{cm}^{-1}$, b) $B_o = 2.15$ kG ($K_o = 0.26\ \text{cm}^{-1}$) and $k_q = 0.5\ \text{cm}^{-1}$, c) $B_o = 3.5$ kG ($K_o = 0.42\ \text{cm}^{-1}$) and $k_q = 0.5\ \text{cm}^{-1}$, d) $B_o = 5.0$ kG ($K_o = 0.60\ \text{cm}^{-1}$) and $k_q = 0.5\ \text{cm}^{-1}$, and e) $B_o = -5.0$ kG ($K_o = -0.60\ \text{cm}^{-1}$) and $k_q = 0.1\ \text{cm}^{-1}$,

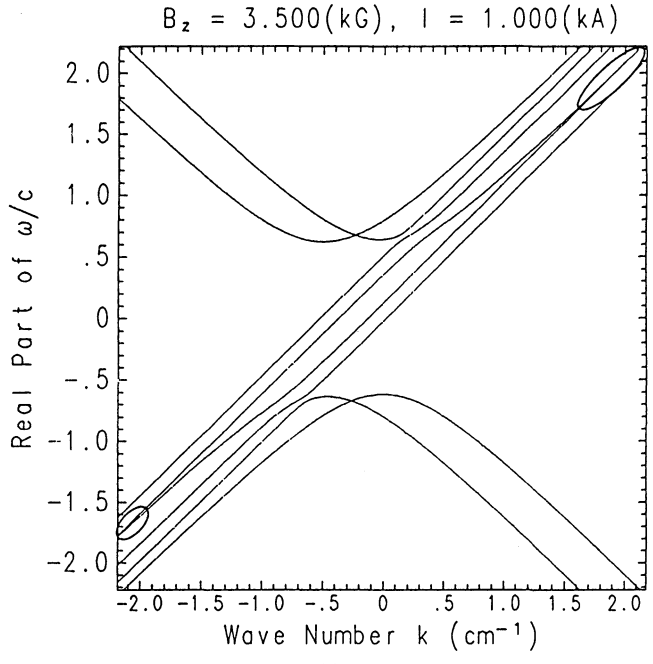

(c)

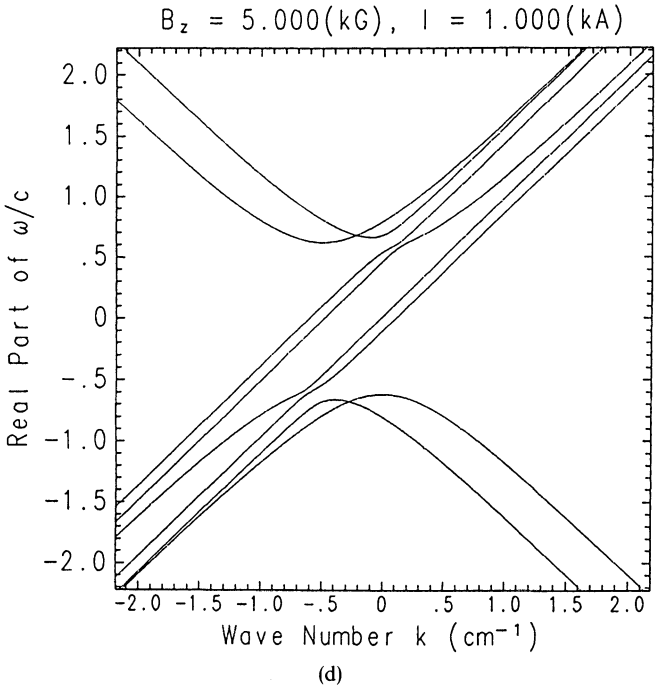

(d)

FIGURE 4 (*Continued*)

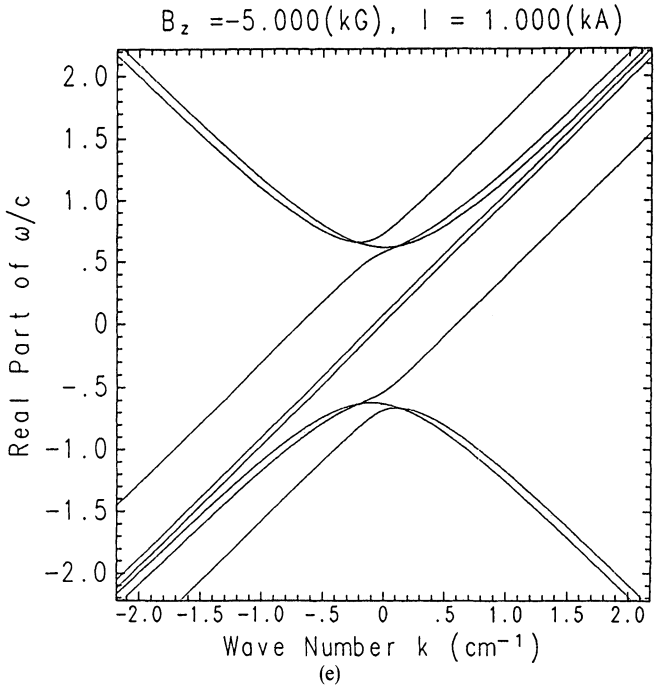

(e)

FIGURE 4 (*Concluded*)

($K_o = 0.39\ \text{cm}^{-1}$) and $B_o = 3.5$ kG ($K_o = 0.41\ \text{cm}^{-1}$). For some values of B_o, the RHCP wave intersects the beam line two times as indicated by temporal growth rates at two separate regions of wave number k for a given axial magnetic field. The growth rate and the range of unstable values of k increases as K_o approaches $K_{\text{crit},3}$. The stability boundaries predict that the three-wave instability is present for $K_{\text{crit},3} = 0.35\ \text{cm}^{-1} < K_o < K_{\text{crit},4} = 0.41\ \text{cm}^{-1}$ (2.95 kG $< B_o <$ 3.5 kG). Numerical results for $I_b = 1$ kA are in excellent agreement with the theory.

Figure 7 plots the temporal growth rate versus k in the orbit-unstable region for $B_o = 2.15$ kG ($K_o = 0.26\ \text{cm}^{-1}$). The region of instability covers both positive and negative values of wave number k, even at regions where the beam lines are far from the waveguide mode. Thus, the unstable growth rate is the result of unstable beam orbits in the stellarator and guide fields, irrespective of the electromagnetic waves.

As the beam current increases, the numerically determined stability regimes deviate from the analytic stability boundaries derived with $I_b = 0$. Figures 8–10 are plots of temporal growth rate as a function of wave number k for $I_b = 10$ kA. Figure 8 plots the temporal growth rates in region I, for $B_o = -1.0$ kG ($K_o = -0.12\ \text{cm}^{-1}$), $B_o = 0$, $B_o = 1.0$ kG ($K_o = 0.12\ \text{cm}^{-1}$), and $B_o = 1.3$ kG ($K_o = 0.156\ \text{cm}^{-1}$).

Figure 9 plots temporal growth rates versus k in the three-wave unstable region II, for $B_o = 3.0$ kG ($K_o = 0.36\ \text{cm}^{-1}$), $B_o = 3.25$ kG ($K_o = 0.39\ \text{cm}^{-1}$), $B_o = 3.5$ kG ($K_o = 0.41\ \text{cm}^{-1}$) and $B_o = 3.85$ kG ($K_o = 0.45\ \text{cm}^{-1}$). The range of B_o for the three-wave unstable region II at zero beam current is 2.95 kG $< B_o <$ 3.5 kG. For current of $I_b = 10$ kA, the dispersion relation shows that the three-wave unstable

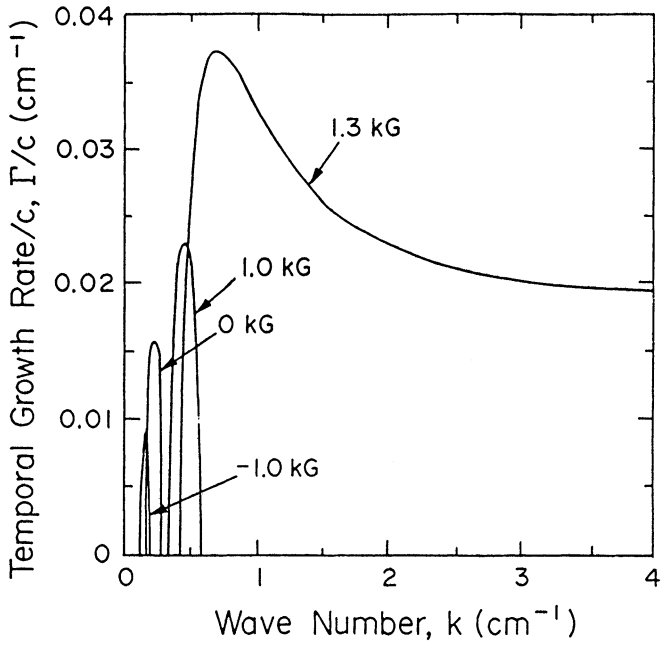

FIGURE 5 Plots of the temporal growth rate versus k in three-wave unstable region I, for current $I_b = 1$ kA and a) $B_o = -1.0$ kG ($K_o = -0.12\ \text{cm}^{-1}$), b) $B_o = 0$, c) $B_o = 1.0$ kG ($K_o = 0.12\ \text{cm}^{-1}$) and d) $B_o = 1.3$ kG ($K_o = 0.156\ \text{cm}^{-1}$).

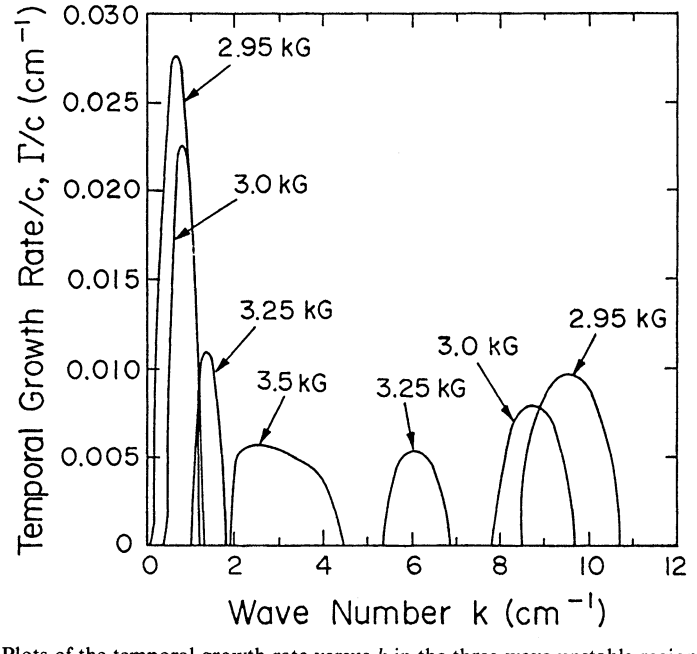

FIGURE 6 Plots of the temporal growth rate versus k in the three-wave unstable region II, for current $I_b = 1$ kA and a) $B_o = 2.95$ kG ($K_o = 0.35\ \text{cm}^{-1}$), b) $B_o = 3.0$ kG ($K_o = 0.36\ \text{cm}^{-1}$), c) $B_o = 3.25$ kG ($K_o = 0.39\ \text{cm}^{-1}$) and d) $B_o = 3.5$ kG ($K_o = 0.41\ \text{cm}^{-1}$).

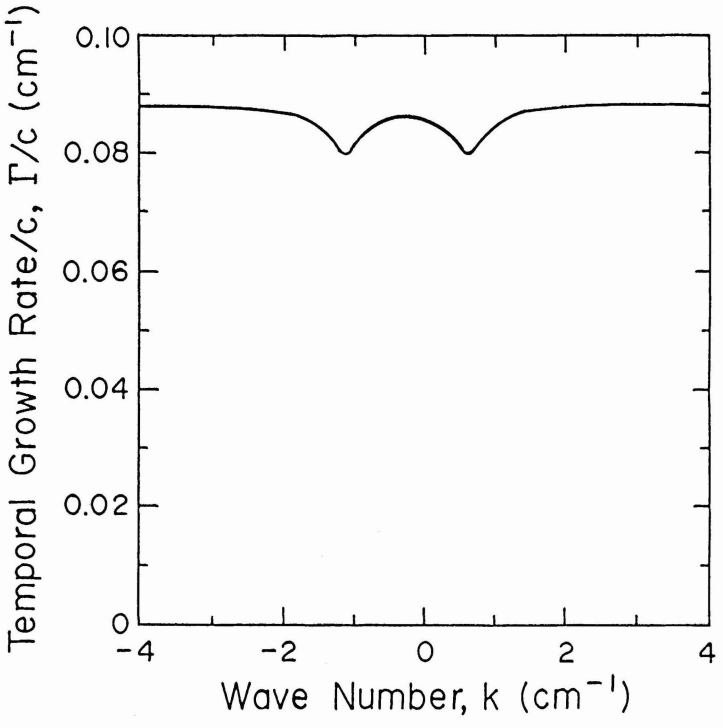

FIGURE 7 A plot of the temporal growth rate versus k in the orbit unstable region, for current $I_b = 1$ kA and $B_o = 2.15$ kG ($K_o = 0.26$ cm^{-1}).

regime extends beyond $B_o = 3.5$ kG to $B_o = 3.85$ kG, where the analytic ($I_b = 0$) expressions predict stability.

Figure 10 plots the temporal growth rate versus k in the orbit-unstable region for $B_o = 2.15$ kG ($K_o = 0.26$ cm^{-1}). Here the region of instability covers essentially all values of wave number k. Note that the dispersion relation predicts orbit instability, i.e., finite growth rate at $k = 0$, for $B_o = 2.95$–3.25 kG, outside of the unstable values 1.32 kG $< B_o <$ 2.95 kG predicted by the analytic stability conditions.

A summary of peak temporal growth rates as a function of normalized guide field K_o for $I_b = 10$ kA is shown in Figure 11 for $\gamma_o = 5$, $\gamma_o = 7.5$ and $\gamma_o = 10$. The group of curves on the left belong to unstable region I and the group of curves on the right belong to unstable region II. The gap separating the two groups of curves corresponds to the orbit-unstable region. Plots of the group velocity as a function of K_o are shown in Figure 12. Those values plotted are associated with the growth rates of Figure 11. The group velocity approaches the beam velocity in three-wave unstable region II.

In all calculations, the effect of induced fields due to image charges and image currents (see Eqs. 10a–b) on the growth rates is small. For current of 1 kA, the induced fields changed the growth rate by 1–2%. For 10 kA, the induced fields changed the growth rate by about 5%.

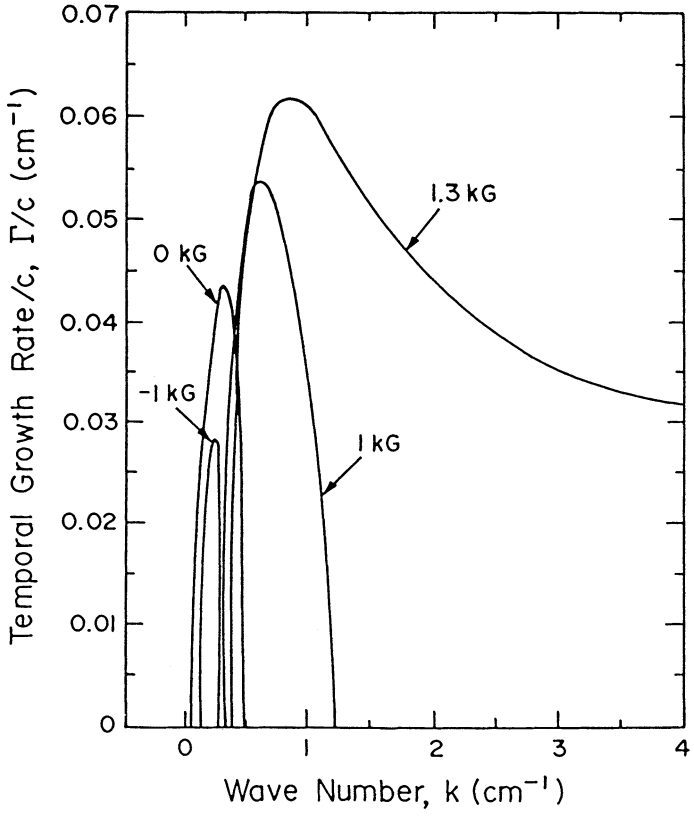

FIGURE 8 Plots of the temporal growth rate versus k in three-wave unstable region I, for current $I_b = 10$ kA and a) $B_o = -1.0$ kG ($K_o = -0.12\,\mathrm{cm}^{-1}$), b) $B_0 = 0$, c) $B_o = 1.0$ kG ($K_o = 0.12\,\mathrm{cm}^{-1}$) and d) $B_o = 1.3$ kG ($K_o = 0.156\,\mathrm{cm}^{-1}$).

We also examine the effect of the waveguide radius r_g on the three-wave instability. As the guide radius is increased, the waveguide cut-off frequency $\mu_{11}c$ decreases. For the three-wave unstable region I, the intersection of the waveguide mode and one of the beam lines in Eq. (28) can occur for negative values of wave number k. When this occurs, the phase velocity is negative and group velocity is positive but reduced in value. Figure 13 plots the temporal growth rate and the group velocity as a function of K_o for $r_g = 5$ cm and $I_b = 10$ kA, while keeping all the other parameters the same as in Table I.

4.2 Comparison of analytic and numerical results

The analytical expressions for the temporal growth rates for the two regions of the three-wave instability are given in Eqs. (47) and (49). Figure 14 is a comparison of the maximum temporal growth rate as a function of the normalized guide field K_o for the values obtained from the numerically solved full dispersion relation (solid

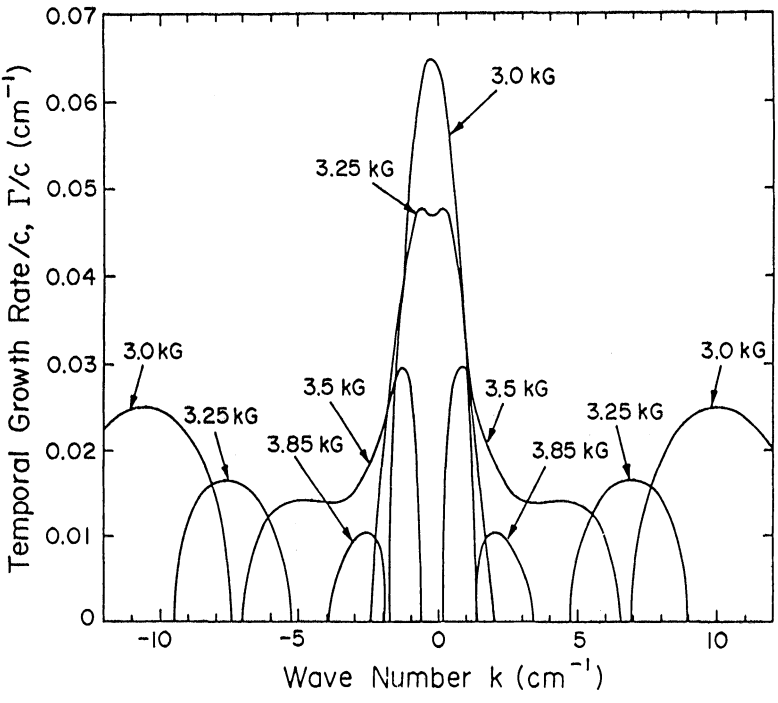

FIGURE 9 Plots of the temporal growth rate versus k in the three-wave unstable region II, for current $I_b = 10$ kA and a) $B_o = 3.0$ kG ($K_o = 0.36\ \text{cm}^{-1}$), b) $B_o = 3.25$ kG ($K_o = 0.39\ \text{cm}^{-1}$), c) $B_o = 3.5$ kG ($K_o = 0.41\ \text{cm}^{-1}$) and d) $B_o = 3.85$ kG ($K_o = 0.45\ \text{cm}^{-1}$).

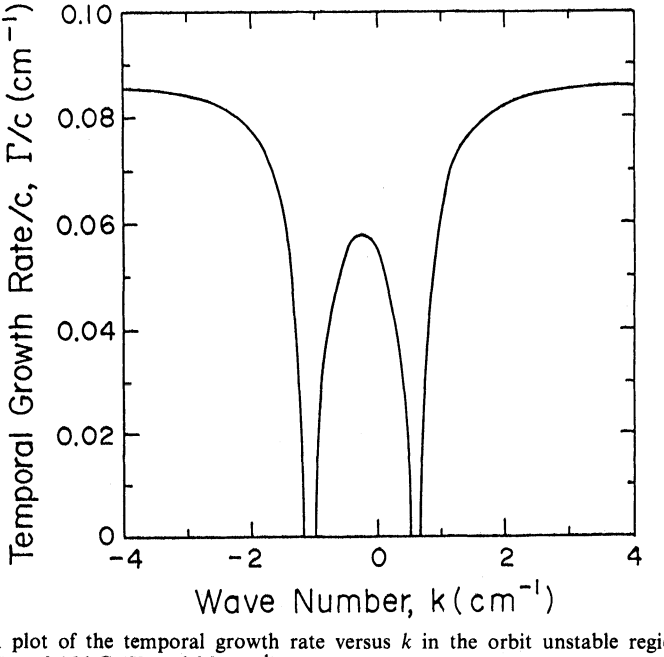

FIGURE 10 A plot of the temporal growth rate versus k in the orbit unstable region, for current $I_b = 10$ kA and $B_o = 2.15$ kG ($K_o = 0.26\ \text{cm}^{-1}$).

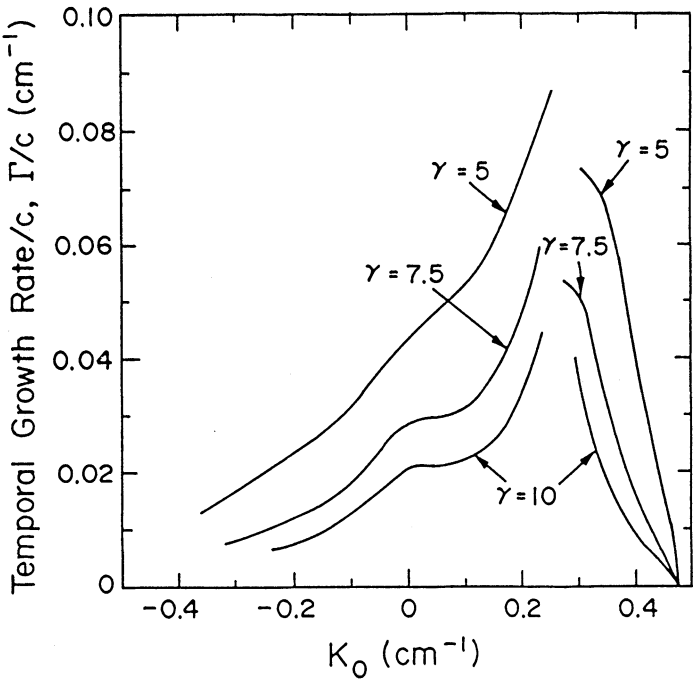

FIGURE 11 Peak values of the temporal growth rate as a function of normalised guide field K_o for $\gamma_o = 5$, 7.5 and 10 with current $I_b = 10$ kA.

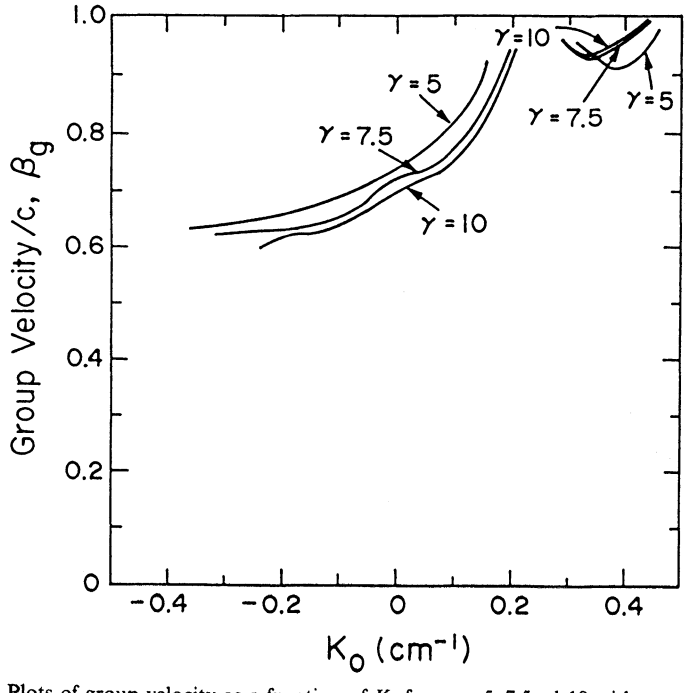

FIGURE 12 Plots of group velocity as a function of K_o for $\gamma_o = 5$, 7.5 ad 10 with current $I_b = 10$ kA.

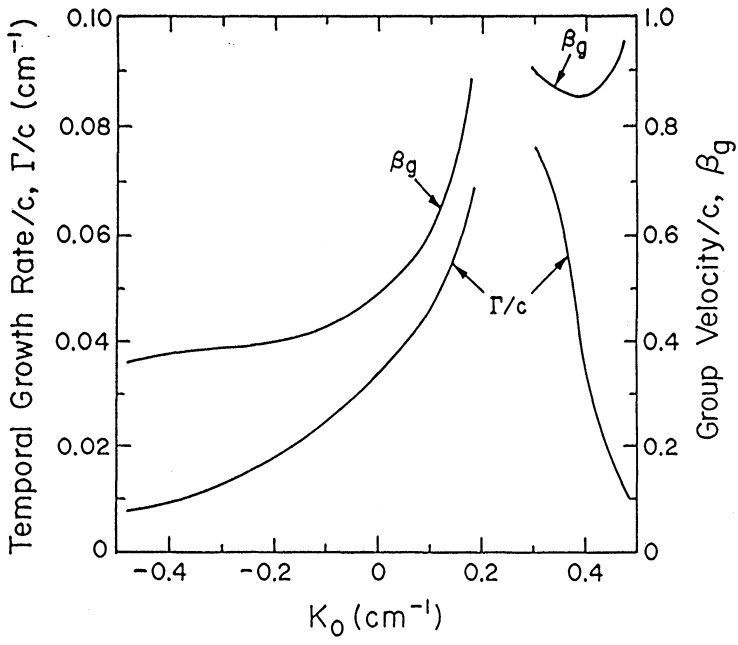

FIGURE 13 Plots of the temporal growth rate and the group velocity as a function of K_o for $r_g = 5$ cm and current $I_b = 10$ kA, while keeping other parameters the same as in Table I.

curves) and from the analytical expressions (dashed curves) for current $I_b = 1$ kA. The agreement between the analytical and numerical results of the temporal growth rates is good as long as $\Delta\omega_2/c > \Gamma/c$; see Eqs. (44)–(49). On the dispersion diagram, $2\Delta\omega_2/c$ is the difference in frequency/c of the beam lines (28) that could go unstable. To illustrate the case $\Delta\omega_2/c > \Gamma/c$, we take $K_o = -0.36$ cm^{-1} ($B_o = -3$ kG). The numerical result of the temporal growth rate is $\Gamma/c = 4.3 \times 10^{-3}$ cm^{-1}, which is much smaller than $\Delta\omega_2/c = 0.25$. The analytical result for the temporal growth rate is also $\Gamma/c = 4.3 \times 10^{-3}$ cm^{-1}. As $\Delta\omega_2/c$ decreases and Γ/c increases, the analytical expressions for the growth rate becomes less accurate. At $K_o = 0.12$ cm^{-1} ($B_o = 1$ kG), $\Delta\omega_2/c = 8.2 \times 10^{-2}$, which is comparable to Γ/c. The analytical expression for the growth rate, $\Gamma/c = 2.50 \times 10^{-2}$ cm^{-1}, is 8% larger than the numerical result of $\Gamma/c = 2.30 \times 10^{-2}$ cm^{-1}.

5. CONCLUSIONS

The addition of stellarator windings to an axial guide field was proposed as a method of transporting a high current beam in a curved geometry with a high tolerance to energy mismatch.[1] The stability properties of such configurations have been clarified in the present study, which included the beam centroid motion, the electromagnetic waveguide modes, expressed in terms of right-hand circularly polarized (RHCP) and

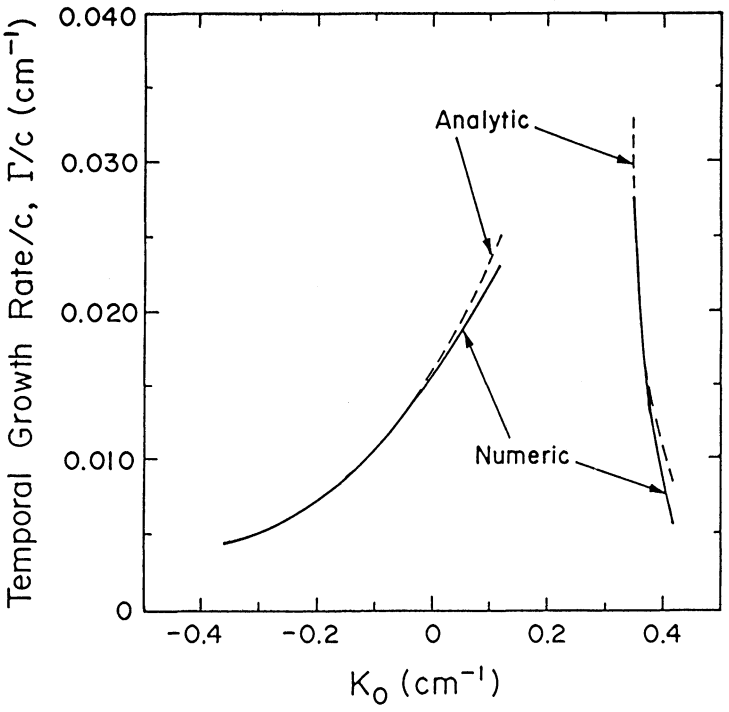

FIGURE 14 Comparison of the maximum temporal growth rate as a function of K_o for the values obtained from the numerically solved full dispersion relation (solid curves) and from the analytical expressions (dashed curves) for the parameters in Table I with current $I_b = 1$ kA.

left-hand circularly polarized (LHCP) waves, and the induced image forces on the conducting boundaries, in addition to the external magnetic fields.

We find five operating regimes: i) two physically distinct three-wave unstable regimes, ii) an orbit-unstable regime, in which the beam centroid is unstable independent of the electromagnetic waveguide modes and iii) two stable regimes. We have obtained analytical expressions for the boundaries of the various stability regimes in parameter space and have presented algebraic expressions for the growth rates in each of the two three-wave unstable regimes. These analytical results are valid in the limit of low beam current, when the RHCP and LHCP waves decouple, and are in good agreement with those obtained via numerical solutions of the full dispersion relation.

The three-wave interaction can be unstable when the RHCP and LHCP waveguide modes are not simultaneously excited as given in Eq. (45). The uncoupled dispersion relation has been shown to produce results that are in close agreement with those of the full dispersion relation. The simplified dispersion relation is not valid, however, when the coupling between the RHCP and LHCP waves is strong, as in the orbit unstable regime. In three-wave unstable region II, the coupling is strong only at high current. The growth rates in this regime, for example, from the full (coupled)

dispersion relation are about 20–30% larger than from the uncoupled dispersion relation for $k_w = 0.5\ \text{cm}^{-1}$ and $I = 10$ kA. In three-wave unstable region I the growth rate associated with coupled RHCP and LHCP waves is essentially the same as the growth rate associated with RHCP or LHCP waves. The coupling of the RHCP and LHCP waves can be detected by the wavenumbers associated with the instability. The instability occurs at k and $-(k + k_q)$ for coupled dispersion relation; while the instability occurs at k when only the RHCP wave is unstable and at $-k$ when only the LHCP wave is unstable.

These results suggest that the three-wave instability can be avoided by appropriately choosing the various parameters. Results show that as the beam energy increases, the stability conditions become more restrictive. In such cases, it may be necessary to decrease the quadrupole gradient, $B_q k_q$, quadrupole wave number k_q and/or increase the value of the guide field B_o in order to remain in the stable regime.

ACKNOWLEDGMENTS

This work is supported by the Defense Advanced Research Projects Agency and the Office of Naval Research. We also like to thank D. Chernin, A. Mondelli and T. Hughes for their insight and T. Swyden for his assistance.

REFERENCE

1. C. W. Roberson, A. Mondelli and D. Chernin, *Phys. Rev. Lett.*, **50**, 507 (1983).
2. P. Sprangle and C. A. Kapetanakos, *Part. Accel.*, **18**, 203 (1986).
3. T. P. Hughes and B. B. Godfrey, *Phys. Fluids*, **29**, 1698 (1986).
4. B. Levush, T. M. Antonsen, W. M. Manheimer and P. Sprangle, Naval Research Laboratory Memorandum Report 5471 (1984) and *Phys. Fluids*, **28**, 7 (1985).
5. P. Sprangle, C. M. Tang and C. W. Roberson, Nucl. Instrum. Meth., **A239**, 1 (1985).
6. J. Golden, J. Pasour, D. E. Pershing, T. Smith, F. Mako, S. Slinker, F. Moro, N. Orrick, R. Altes, A. Fliflet, P. Champney and C. A. Kapetanakos, *IEEE Trans. Nucl. Sci.*, **NS-30**, 2114 (1983).
7. A. Mondelli, D. Chernin, S. D. Putnam, L. Schlitt and V. Bailey, Proc. Sixth Int'l. Conf. on High Power Part. Beams (Osaka, Japan), (1986).
8. V. Bailey, L. Schlitt, M. Tiefenback S. Putnam, A. Mondelli, D. Chernin and J. Petillo, Proc. 1987 IEEE Part. Accel. Conv., ed. by E. R. Lindstrom and L. S. Taylor, 920 (1987).
9. S. D. Putnam, Proc. 1987 IEEE Part. Accel. Conf., ed. by E. R. Lindstrom and L. S. Taylor, 887 (1987).
10. C. Kapetanakos, L. K. Len, T. Smith, J. Golden, K. Smith, S. J. March, D. Dialetis, J. Mathew, P. Loschialpo and J. H. Chang, *Phys. Rev. Lett.*, **64**, 2374 (1990); C. Kapetanakos (private communication).
11. D. Chernin and T. Hughes (private communication).
12. B. B. Godfrey and T. P. Hughes, "Quadrupole Focusing Instability Growth Rate Expressions", MRC/ABQ-R-1101 (Mission Research Corporation, Albuquerque, NM, Jan. 1988).
13. D. Chernin, *Part. Accel.*, **24**, 29 (1988).